

Investigation of Blade Loads on a Modern High-Speed Lift-Offset Coaxial Helicopter using Coupled Computational Fluid Dynamics / Computational Structural Dynamics

George Jacobellis*

PhD candidate
Rennselaer Polytechnic Institute

Phuriwat Anusonti-Inthra

U. S. Army Research Laboratory

Farhan Gandhi

Professor
Rennselaer Polytechnic Institute

ABSTRACT

Three different aerodynamic models are used to analyze a modern lift-offset coaxial helicopter in high-speed cruise. The first and simplest method, dynamic inflow, is used along with Computational Structural Dynamics (CSD) to determine the trimmed flight conditions at speeds up to 250 kt. Two higher order models, the Viscous Vortex Particle Method (VVPM) and Computational Fluid Dynamics (CFD) are then used to evaluate the same trimmed condition at a speed of 230 kt. VVPM is capable of capturing the rotor to rotor interference from first-principles at a significantly lower cost than CFD. The high resolution CFD solution revealed significant deviations in the airloads from the values obtained with the first two methods.

NOTATION

(x, y, z)	Vehicle coordinate system, oriented positive (aft, starboard, up)
F	Rotor force
H	Rotor longitudinal force, positive aft
LOS	Lift-offset (%)
M	Rotor moment
Nr	Nominal rotor speed
P	Power
R	Rotor radius
T	Rotor thrust
V_∞	Freestream velocity
ψ	Rotor azimuth angle

INTRODUCTION

The next generation of vertical lift vehicles will reach speeds of 230–300 kt, nearly double that of current operational helicopters. Reaching speeds this high will require a departure from the single main rotor/tail rotor configuration and adoption of a new platform. Slowed rotor compound and lift-offset coaxial configurations have received significant interest in recent years. Both of these configurations operate at high advance ratios (0.8 and above) due to the high forward speed and the slowing of the rotor to keep the advancing tip Mach number below 1. As the advance ratio increases, the size of the reverse flow region (where the air flows from the trailing edge of the blade to the leading edge) grows and the ability of the retreating side of the rotor to generate lift decreases.

Presented at the AHS Aeromechanics Specialists' Meeting, Holiday Inn at Fisherman's Wharf, San Francisco, California, January 16-19, 2018 Copyright © 2018 by the American Helicopter Society International, Inc. All rights reserved.

*Corresponding author: gjacobellis@gmail.com

While single rotor compound vehicles must use wings or other means to generate lift, lift-offset coaxial helicopters utilize the potential of the advancing side to generate most of the necessary lift, with the retreating side generating less lift. The center of lift of each rotor is located towards the advancing side (hence the name lift-offset) and the two counter-rotating rotors carry equal and opposite roll moments.



Fig. 1. X2 Technology Demonstrator™

The lift-offset coaxial compound helicopter was first demonstrated with the XH-59 in the 1980s. The XH-59 was able to reach speeds in excess of 250 kt and demonstrated good maneuverability and handling qualities. (Refs. 1–7) Several issues with the XH-59, such as poor performance and high vibrations at high speeds, were later improved upon with the X2 Technology Demonstrator™ (Refs. 8–11), shown in Figure 1, and its derivatives. The X2 is designed to cruise at speeds up to 250 kt and advance ratios up to 0.8. At these conditions, the difference in incident velocity between the

advancing and retreating side is large, and can lead to large lift and rolling moments generated on the advancing side. If left unchecked, the moments carried by the individual rotors would become excessive, leading to unacceptably large loads in the blade roots and rotor shaft. In practice the blade pitch on the retreating side must be increased to keep the individual rotor roll moments at reasonable levels (lift-offset below 30% in the case of the X2).

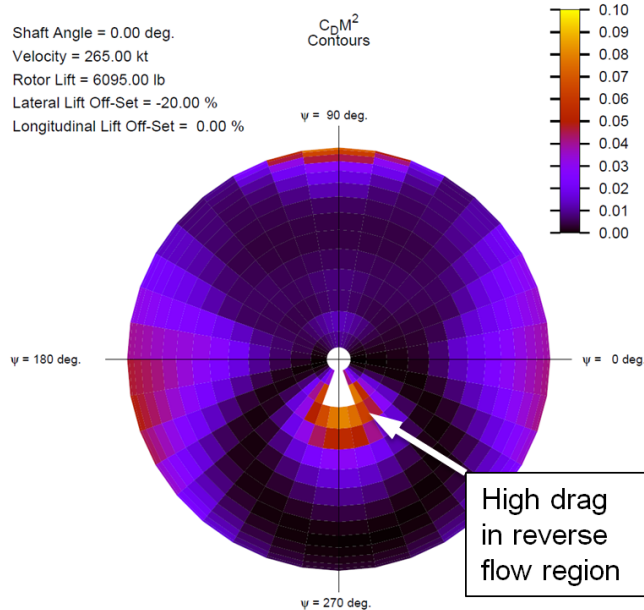


Fig. 2. Drag on X2 Technology Demonstrator™ Rotor (Ref. 8)

The operating conditions of the X2 also lead to the retreating blades experiencing a substantial reverse flow velocity at their most inboard locations. On the XH-59 the inboard section of the blade had large chord, and high twist, standard for rotors to achieve good hover performance. These sections were not designed to operate in reverse flow, and when subjected to it, will create regions of separated flow, leading to very high drag and unsteady loading. One of the key improvements made with the X2 was replacing the traditional sharp trailing edge airfoils on the inboard section of the blade with cambered elliptical airfoils which have much lower drag than a sharp trailing edge airfoil in reverse flow conditions. Additionally the chord and twist are both reduced on the inboard section of the rotor. Despite these changes high drag still persists in the reverse flow region, as shown in Figure 2.

Quantifying the performance of the rotor blades in this region is a challenge. Most reduced order models for rotorcraft analysis rely on airfoil tables for lift, drag, and moment coefficients. Airfoils undergoing dynamic pitching and changes of incident velocity can depart significantly from their steady performance, however these unsteady effects are often neglected when using airfoil data for rotor performance and load calculations. Furthermore, airfoil tables are often based on wind tunnel tests or two-dimensional computational fluid dynamics (CFD) simulations at forward angles of attack. Few

wind tunnel experiments capture the airfoil data in reverse flow and using CFD to obtain accurate reverse flow performance is much more difficult than forward flow as the performance of the airfoil is highly sensitive to separation and attachment points. There have been several recent efforts to characterize airfoils in the reverse flow region. An experimental and CFD study of the NACA 0012 and DBLN526 in reverse flow at Reynold number of 110,000 was conducted by Lind et. al. (Ref. 12). This work was followed up by (Ref. 13) in which the various vorticies produced by a sharp trailing edge rotor blade were characterized.

Hodora et. al. compared several different computational methods with experimental measurements of sharp trailing edge blades in reverse flow in Ref. 14. They found that the flow was highly separated and that using detached eddy simulation improved the CFD predictions. They also pointed out that slight changes in the geometry of the blade and grid near the trailing edge can result in large changes in the resultant loads obtained by CFD.

Mayo et. al (Ref. 15) experimentally tested a stationary rotor blade at several reverse flow yaw angles. It was shown that there is a strong attached vortex that forms as the flow separates over the sharp trailing edge of the blade in reverse flow. The presence of the vortex was shown to alter the loads expected based only on the yaw angle, and accounting for the presence of the vortex via the Polhamus equation resulted in accurate loads prediction.

Hiremath (Refs. 16, 17) conducted flow visualization on a rotor in a wind tunnel and revealed an attached vortex similar to the one shown on the static blades in Ref. 15 as the rotating rotor blade passed through the reverse flow region.

In addition to the flow near the blade, reduced order wake models also have other shortcomings: while the dynamic inflow model is fairly accurate for single rotor performance predictions, it cannot accurately model detailed wake features such as blade vortex interactions. Vortex wakes, while being well suited to account for interference effects, rely on several empirical factors such as the vortex decay rate and viscous core size. Additionally, they do not include viscous effects outside of these empirical corrections, which are important when a rotor wake interacts with a fuselage or other rotors. The Viscous Vortex Particle Method (VVPM) is similar to free vortex wake methods, but includes viscous forces in its formulation, allowing it to model viscous effects better while relying on fewer empirical parameters and still running at the speed of a reduced order model (Ref. 18). In theory, high fidelity CFD models should provide better prediction of the viscous, unsteady, and interference effects, but limits on computational resources may necessitate compromising the accuracy of the solution.

Yeo and Potsdam (Ref. 19) compared the ability of a vortex wake model and coupled CFD/CSD to predict the measured blade and pitch link loads on a UH-60 rotor in a high advance ratio condition. They found that modal damping and a non-linear lag damper model are important for better predictions of the loads at these conditions. With these improvements the

CFD/CSD simulation was able to capture many difficult phenomena such as stall events on the retreating blade at high advance ratio, but even with coupled CFD/CSD there were significant deviations between the predicted and measured loads.

Several researchers have used reduced order models to investigate high-speed coaxial rotors. In Ref. 20 Johnson compared CAMRAD II models of the XH-59 and X2 to flight test data, showing that good predictions of rotor and aircraft performance could be achieved with vortex wakes. Kim et. al. used a vorticity transport model (VTM) to study the aerodynamic interactions occurring on a coaxial helicopter with a rigid rotor having the XH-59 geometry in Ref. 21. The VTM is different from the VVPM in that it still requires a grid to capture the flow field. The fuselage aerodynamics were computed with a vortex panel method requiring specification of the separation points.

Other researchers have performed wind tunnel experiments on Coaxial rotors. Cameron et. al. performed wind tunnel tests of a model scale coaxial rotor with untwisted, constant cross section blades in Ref. 22 and Schmaus et. al. showed good free wake predictions of the steady performance of the same rotor in Ref. 23. Cameron et. al compared measurements of the transient loads and deflections on a coaxial rotor in hover with CAMRADII free wake predictions in Ref. 24. A study of the rotor and fuselage aerodynamic interaction was conducted by Passe et. al. In Ref. 25. Passe created a CFD model of the X2 from publicly available data and ran the CFD simulation using Helios (Ref. 26), which is a framework for coupling CFD and structural dynamics for rotorcraft. CAMRAD II was used for the structural model and NSU3D and Overflow were used for the CFD simulation. While the X2 has a top speed of 250kt, trimmed solutions were only able to be obtained up to 150 kt.

The current work will use Dynamic inflow to trim a modern coaxial helicopter (The X2TD) at high speeds (up to 250 kt) as well as compare selected cases with a VVPM and full CFD solution. One of the key goals is to determine how the unsteady CFD loads compare with the steady aerodynamic loads generated with the reduced order models, especially in the reverse flow region.

APPROACH

The X2 has a counter rotating coaxial rotor system. Important rotor properties are summarized in Table 1. The blades also have 2° precone, which was estimated from images of the X2.

Table 1. Properties

Gross Weight	5,300 lb
Rotor radius	13.2 ft
Blades per rotor	4
Rotor separation	1.5 ft
Precone	2°

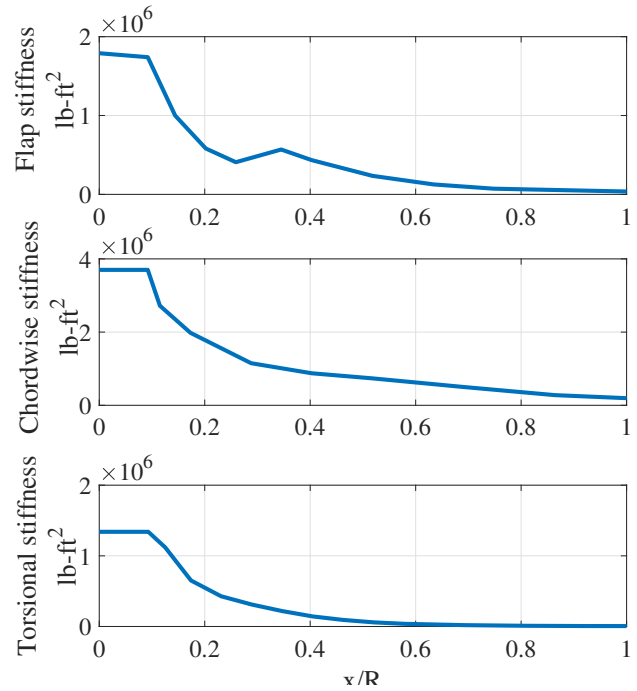


Fig. 3. Rotor blade structural properties

Structural Model

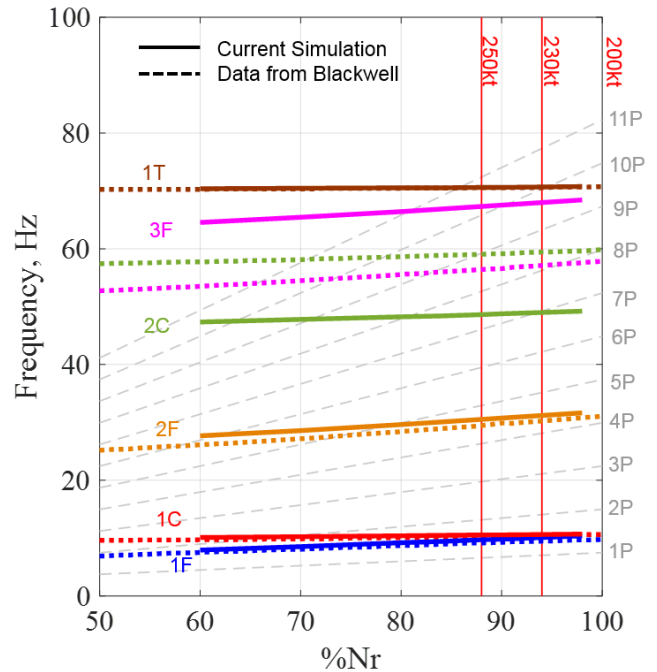


Fig. 4. X2 fan plot, current model compared to Ref. 9

The structural properties of the blades are the same as used in Ref. 25 which were estimated by scaling down the properties of the XH-59 blades. The structural properties are shown in Figure 3. RCAS, the structural solver, models the blades as 1D nonlinear finite element beams using a multi-body dynamic formulation (Ref. 27). The blade is modeled as a one-

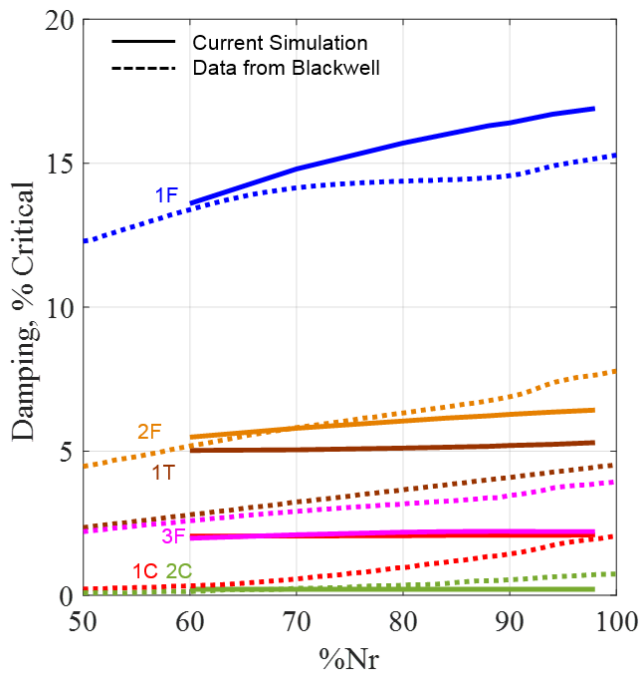


Fig. 5. X2 damping plot, current model compared to Ref. 9

dimensional beam divided into 18 elements, which are more closely spaced near the root. The structural model is validated by comparing the current model's fan plot (Figure 4) with the data given in Ref. 9. Figure 4 shows that the first flap, lag, and torsional frequencies of the current model are very close to those of Sikorsky's model given in Ref. 9. At 100% Nr they differ by 4%, 2.7%, and 0.7%, respectively. The operational rotor speeds for 200 kt (and under), 230 kt, and 250 kt are also marked on the fan plot. The 1st torsional mode is close to the 10/rev and 11/rev excitation frequencies at 230 and 250 kt, respectively. Additionally, the 2nd chordwise mode is close to the 7/rev excitation frequency at 230 kt.

The damping plot for the current model is shown in Figure 5 along with data from Ref. 9. The damping (percent critical) for the 1st flap, 1st chordwise, and 1st torsional modes reported in Ref. 9 are approximately 15%, 2%, and 5%, respectively. The modal damping for all modes in the current model was set to values from 2-5% to more closely match the values shown in Ref. 9.

Aerodynamic Model

The aerodynamic properties of the blade were taken from Refs. 8 and 28. Airfoils similar to that found on a modern coaxial helicopter such as the X2 were used, including double ended airfoils on the inboard section of the blade. Figure 6 shows the blades planform, twist and thickness distribution. On the outer half of the span, the airfoil sections are placed with the quarter chord along the elastic axis of the blade (the zero coordinate in the top of Figure 6). Inboard of 50% radius the placement of the airfoil sections is gradually moved forward such that at the root of the blade, the center of the airfoil

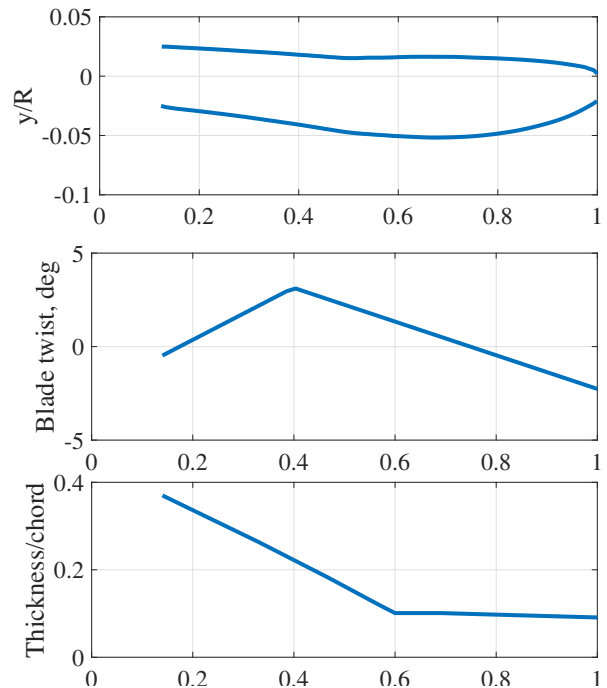


Fig. 6. X2 Rotor blade geometry

is along the elastic axis. Having the elastic axis at the 50% chord point reduces the torsional moments due to the shifting of the aerodynamic center as the blade moves into and out of reverse flow.

Reduced order models

The dynamic wake and VVPM simulations use a lifting line model including airfoil tables which tabulate the steady force and moment coefficients. The airfoil force and moment coefficients were obtained using steady, two dimensional Reynolds Averaged Navier-Stokes simulations at a Mach number equal to the hover Mach number, with the exception of the DBLN526. The data for the DBLN526 was taken from Ref. 12. The lift to drag ratio of the airfoils used is shown in Figure 7. The dynamic wake and VVPM simulations were run using the Rotorcraft Comprehensive Analysis System (RCAS) which has been validated for several types of rotors (Ref. 20). The geometry of the RCAS model is shown in Figure 8. The dynamic wake is a 12×12 state Peters-He dynamic inflow model. Both the dynamic wake and VVPM solution use a timestep of 2° . The VVPM simulation uses 20 equally spaced vortex particles along the blade span. These particles are released every timestep and are free to convect with the local flow. at each time step the influence of each particle on all of the other particles is used to update the local flow and determine the motion of the particles. The VVPM is described in detail in Ref. 18.

CFD/CSD Model

In the current study, the RCAS structural model is used along with 12×12 state Peters-He dynamic inflow to obtain the

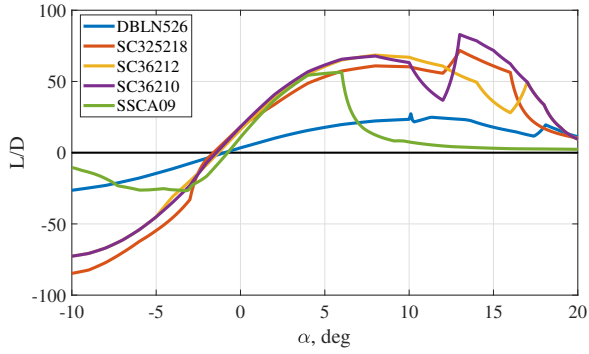


Fig. 7. Lift to drag ratio of airfoils at moderate angles of attack

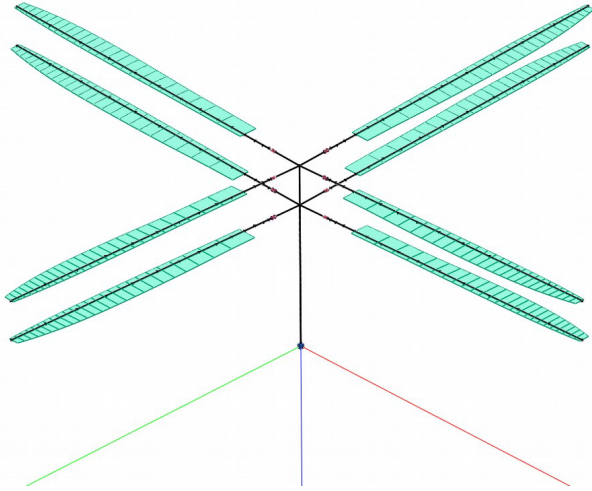


Fig. 8. RCAS representation of the structural and aerodynamic model

rotor trim parameters and blade deformation which are transferred subsequently to Helios (Version 7.1.0) (Ref. 26) to perform CFD simulations. The Helios computational platform automatically transfers relevant information between several modules including near-body CFD solvers, an off-body solver, and RCAS. For this study kCFD is used as the near-body flow solver and DES (Detached Eddy Simulation) is used for the turbulence modeling. The near-body CFD solver is capable of resolving the boundary layer, flow separation, and other 3D effects close to all of the surfaces. A total of 10 near body meshes for the rotors and hubs are used. The representation of the blade and the surrounding near-body grid is shown in Figure 9. The near-body grids for the blades extend to about one chord length from the surfaces and contain approximately 1.4 million gridpoints each. The blade near-body grids include blade deformation and rotor pitch control, while the near body-grids for the hub do not accommodate any deformation.

The off-body CFD solver SAMCART, is based on a high order Cartesian flow solver. The extent of the off-body grid zone is $(12.5 \times 12.5 \times 12.5$ rotor diameters). The AMR algorithm uses vorticity and/or circulation threshold to refine the off-body grid. Up to fifteen levels of refinement is used to

Hub gridpoints (upper)	634,010
Hub gridpoints (lower)	247,268
Near body nodes	1,379,016
Off body gridpoints	231,635,178
CFD timestep	0.000079 sec (0.2°)

resolve the tip vortices and other vortical features. A typical run has approximately 230 million gridpoints for the off-body solver. On approximately 1,000 processors a single rotor revolution takes 8-12 hours of runtime.

Table 2 lists the size of the near and off body grids as well as other parameters of the CFD simulation.

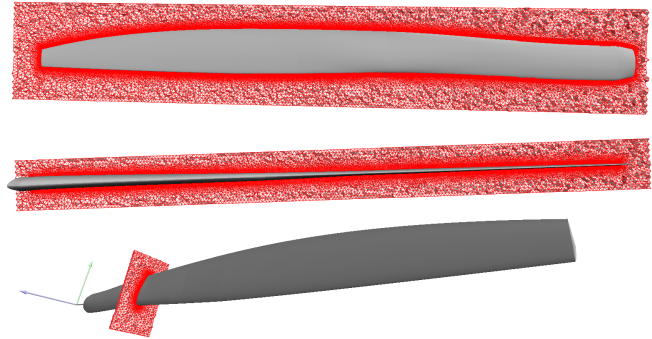


Fig. 9. Near body grid

ANALYSIS

The rotor lift-offset can be thought of as the lateral location of the center of lift of each rotor. It is expressed as a percent of the rotor radius (e.g. 20%) or fraction of the rotor radius (e.g. 0.2). It is calculated as shown in equation 1

$$LOS = \frac{\Delta M_x}{TR} \quad (1)$$

where ΔM_x is the difference between the lateral moments between the upper and lower rotor, T is the combined thrust of the two rotors, and R is the rotor radius.

Table 3. Trim variables and targets

Trim variable	Trim target
Collective pitch	Vertical Force = 5,300 lb
Differential collective	Net Torque = 0
Lateral pitch (upper)	Rotor roll moment = 7,143 ft-lb
Lateral pitch (lower)	Rotor roll moment = 7,143 ft-lb
Longitudinal pitch (upper)	Rotor pitch moment = 0
Longitudinal pitch (lower)	Rotor pitch moment = 0

The current model has been trimmed up to 250 kts using RCAS with dynamic inflow. Cylindrical vortex sheet wakes are used to account for the interference between the upper and lower rotors in the Dynamic inflow simulation. The trim

parameters and targets are outlined by Table 3. The current analysis includes the rotors only. The rotor speed is scheduled as indicated in Ref. 8, and is shown in Figure 10. At higher flight speeds the rotor is slowed to keep the advancing tip Mach number at 0.9. In the flight tests, the X2 used a differential lateral schedule which was designed to keep the blade tip clearance above the minimum of 11 inches. This resulted in a lift-offset ranging from about 5% at low speeds (below 100kt) and increasing to about 20% at 250 kt. In Ref. 20, Johnson created a schedule of lift-offset vs. airspeed that fit the flight test data and trimmed each rotor to achieve these specified moments. A similar method is employed in the current work whereby the roll moments of each rotor are trimmed to specified values. The resulting lift-offset is shown in Figure 10 along with flight test data from Ref 11. Longitudinal trim is achieved via the longitudinal cyclic pitch. The longitudinal moment required by the rotor depends on the pitching moment applied by the horizontal stabilizer (which is a function of the angle of attack). Ref. 11 states that at high speeds the aircraft was generally flown at 2-5° nose up pitch attitude for the best performance. Because the exact fuselage aerodynamics are not yet incorporated, the pitching moments for each rotor are trimmed to zero.

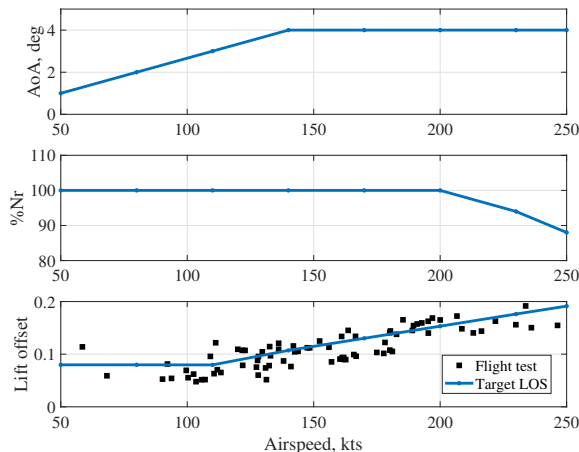


Fig. 10. Angle of attack schedule (top), Rotor speed schedule (middle), and lift-offset target (bottom) compared with data from Ref. 11

The vehicle pitch attitude (also referred to as rotor shaft angle or angle of attack) is specified a priori. As the rotor shaft angle is increased, the rotor power decreases (while rotor H-force and propeller thrust required increase). The relationship between rotor power and shaft angle is explored further in Ref. 29. Figure 12 shows the rotor power compared with flight test data from Ref. 11. In Ref. 20, Johnson altered the pitch attitude of the aircraft to match the power in the test data. In a similar fashion, the current work uses a pitch attitude schedule ranging between 0 and 4 deg that keeps the rotor power close to that achieved during the flight test. This schedule is shown in Figure 10. The controls required for trim across all airspeeds are shown in Figure 11. At high speeds

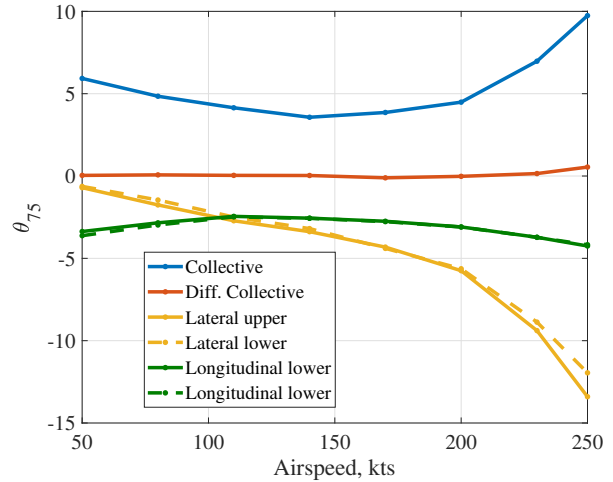


Fig. 11. Controls obtained by trimming with dynamic inflow

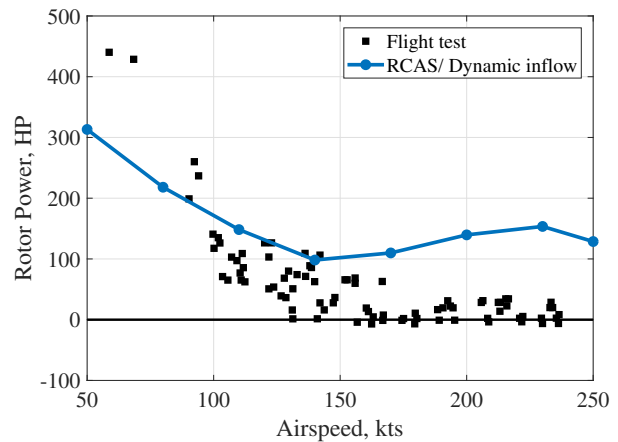


Fig. 12. Rotor power compared with flight test data

controlling lift-offset quickly becomes a problem, as indicated by the drastic increase in the amount of lateral cyclic required above 200 kt. As the forward speed increases from moderate speeds to 200 kt, the amount of lateral cyclic pitch needed to maintain the lift-offset at an appropriate value increases. At speeds above 200 kt when the rotor speed is also decreasing with airspeed, the amount of lateral pitch necessary continues to increase at an even faster rate, reaching about 10° at 250 kt. At all airspeeds, 3-4° of negative longitudinal pitch is needed to counteract the increased lift on the front of the disk and keep the rotor pitching moment equal to zero. The values of differential collective required were small (below 1°) as the differences in the incident velocity encountered by the upper and lower rotor were small compared to that caused by the relatively high forward flight speed.

The root pitch is shown in Figure 13. It is seen on Figure 13 that despite the allowance for lift-offset, the blade experiences large pitches on the retreating side. The elastic deflection of the blade is also shown in figure 13. The torsionally stiff blades are twisted less than 1° (from the root to the tip of the blade). Figure 13 also shows that as the rotor approaches

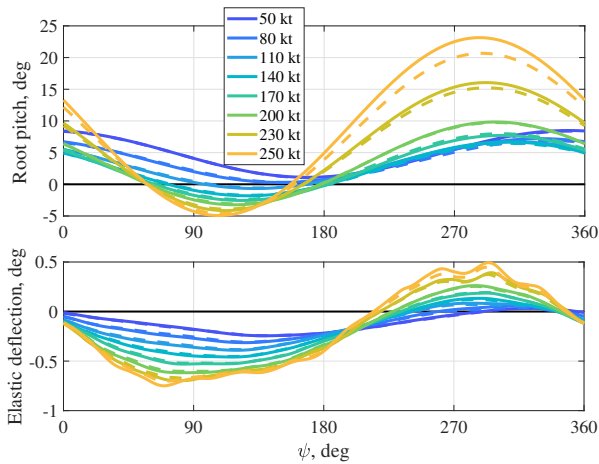


Fig. 13. Root pitch and elastic deflection at 230 kt

the maximum speed of 250 kt, the high frequency torsional oscillations of the blade become large. A slightly slower flight condition, 230 kt was chosen for further analysis with CFD and VVPM.

INVESTIGATION OF HIGH-SPEED FLIGHT CONDITION

Table 4 shows the trim conditions achieved by the dynamic inflow model at 230 kt. These controls were used for the VVPM and CFD simulations. The blade deflections from the dynamic inflow solution were supplied to the CFD model without coupling while the VVPM solution was coupled. The blade flap deflection limits and orientation relative to the oncoming airstream are shown in Figures 14.

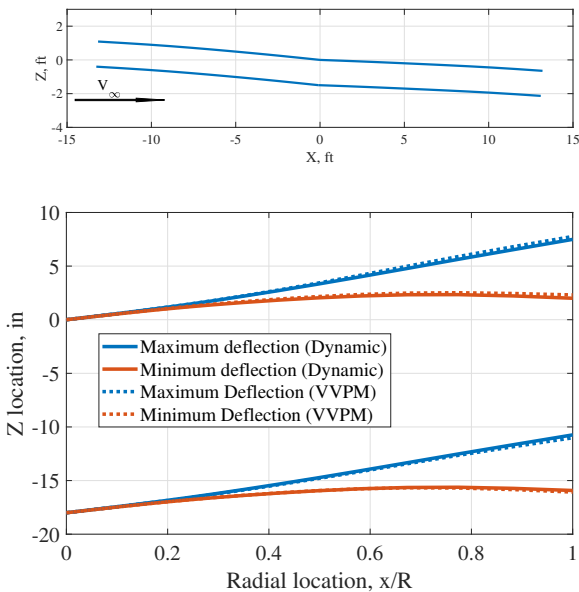


Fig. 14. Blade longitudinal flap deflection (top) and maximum and minimum deflections (bottom) at 230 kt

Table 4. Trim at 230 kt

Pitch	4°
Advance Ratio	0.66
Advancing tip Mach	0.88
Collective	6.17°
Differential collective	0.29°
Lateral (upper/lower)	-8.44° / -7.62°
Longitudinal (upper/lower)	-4.06° / -4.02°
Coning (upper/lower)	1.53° / 1.51°
Lateral flap (upper/lower)	0.5° / 0.5°
Longitudinal Flap (upper/lower)	0.27° / 0.28°

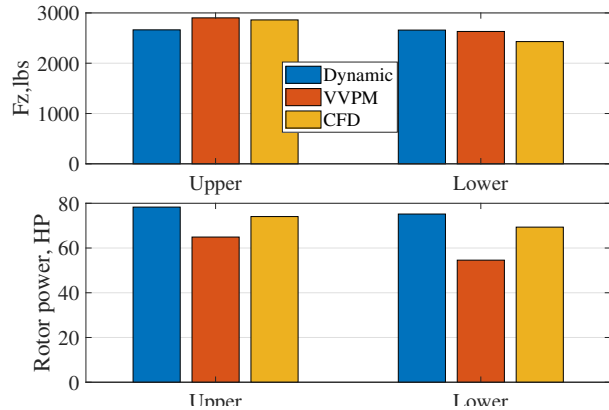


Fig. 15. Comparison of rotor thrust and power

Figure 15 compares the average rotor forces and power for each rotor with the three different methods. The total forces and power are given in Table 5. All three of the inflow models give the same total thrust within 4%, however the thrust of the individual rotors differs by up to 8%. The VVPM predicts a 21% lower power than the Dynamic inflow solution and the CFD predicts 7% lower power.

Table 5. Performance at 230 kt

	Dynamic	VVPM	CFD
Thrust	5,323 lb	5,534 lb	5,291 lb
Power	153.4 HP	119.7 HP	143.4 HP

Figure 16 shows visualizations of the wakes for the CFD and VVPM simulations. The visualization of the CFD simulation shows that there are multiple blade vortex interactions, particularly on the retreating side (lower blade on the left side of the picture and the upper blade on the right side of the picture) where the blade passes through its own tip vortex. The visualization of the VVPM wake shows a qualitatively similar flowfield but lacking the resolution of the CFD solution. The resolution of the VVPM simulation can possibly be improved by increasing the number of timesteps and particles.

Figure 17 shows the convergence of rotor forces and power in the CFD simulation. The solution becomes periodic after about 1 rotor revolution. The periodic solution shows a significant 4/rev (the number of blades per rotor) vibratory component to the forces and power, with a slightly smaller 8/rev

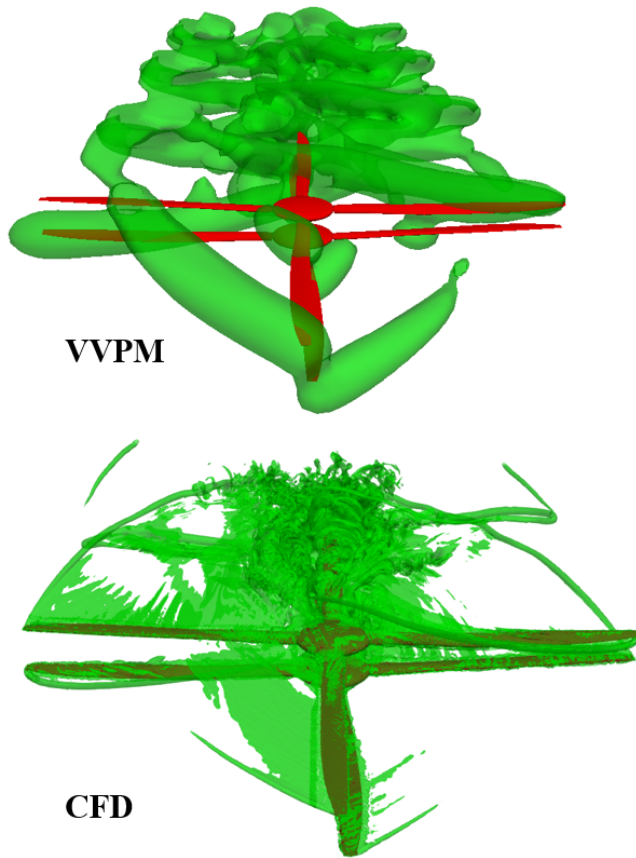


Fig. 16. Iso-surfaces of vorticity magnitude (view from front, looking downstream)

(the blade passage frequency) component also clearly noticeable. The unsteady component of forces and power are larger on the upper rotor because it receives the wake of the lower rotor due to the 4° aft tilt of the rotor system (recall figure 14).

Aerodynamic blade loads

Figures 18, 19, and 20 show the blade lift, drag, and moment for each of the three analysis methods. The lift plot for the CFD simulation was generated by interpolating the pressure forces from the CFD mesh to the same 25 aerodynamic segments as used in the reduced order models. In Figure 18 the lift appears qualitatively similar between the three methods. The lift is mostly concentrated on the advancing side, which is expected for a lift-offset rotor. Regions of negative lift are also visible on the advancing tip and in the reverse flow region, although in the CFD solution the negative lift does not appear on the advancing tip. For the Dynamic inflow and VVPM simulations, the lift near the root (inside of 39% span) where the DBLN airfoil is used is relatively low compared to that seen in the CFD simulation. At 39% span, the airfoil table assignment switches to the SC325218, resulting in a sharp jump in the lift. In the CFD model the blade geometry is smoothly blended between the DBLN and the SC325218 geometry, resulting in a smoother distribution of lift. The lift distributions from CFD in Figure 18 also show evidence of the hub wake

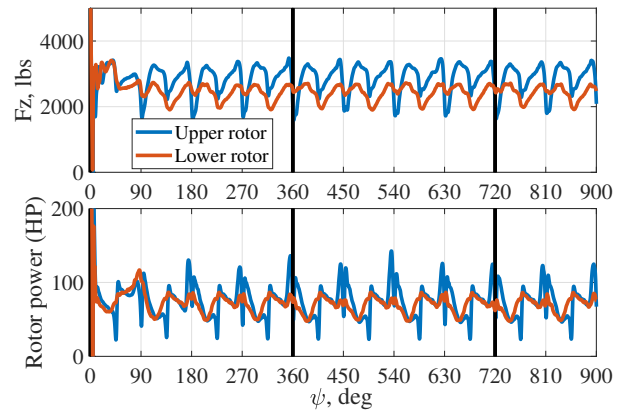


Fig. 17. Convergence of rotor thrust and power

near 0° azimuth on the upper rotor. The effect of blade passage on the lift can be seen in some areas of the VVPM and CFD solutions as small disturbances every 45° (on the retreating side of the upper rotor in the CFD solution, for example).

The drag shown in Figure 19 is also qualitatively similar between the three analysis methods. In the low order models, the drag is greatest between 0° - 90° as this quadrant has low upwash (relative to the front of the disk and a high incident velocity (relative to the retreating side). The drag is negative over much of the retreating side, where the incident velocities are low. As with the lift, sudden changes are observed at 39% span where the assignment of airfoil tables switches. As with the lift, the CFD shows evidence of the hub wake and blade passage events. The CFD solution also shows the region of negative drag (outlined by the bold black line) extending further on the advancing side than it does on the Dynamic wake and VVPM solutions and the highest drag regions on the Dynamic inflow and VVPM solutions (near 45° azimuth) are less prominent in the CFD solution.

Figure 20 shows the pitching moment comparison. Because the DBLN airfoil tables did not include values for pitching moment (moment was not reported in Ref. 12) the value is zero inside of 39% span. The reduced order models predict a smooth variation in pitching moment, with negative values over most of the disk and slight positive values in the reverse flow region and on the retreating side near the blade tips. The CFD simulation shows a similar distribution, although the positive pitching moments generated in the reverse flow region are larger. The positive pitching moments in the reverse flow region are expected as the aerodynamic center shifts to $3/4$ chord and the lift becomes negative in reverse flow. The pitching moments shown in the disk plots are about the blade elastic axis, which is located at 50% chord at the most inboard blade sections (recall Figure 6).

Figure 21 shows the same data as Figure 18 for locations of 25%, 50%, and 75% span for each of the three analysis methods. A strong $1/\text{rev}$ component seen around mid-span correlates with what would be expected from a lift-offset rotor. The differences between the three methods is most visible near 90° azimuth where the lift predicted by CFD is slightly higher

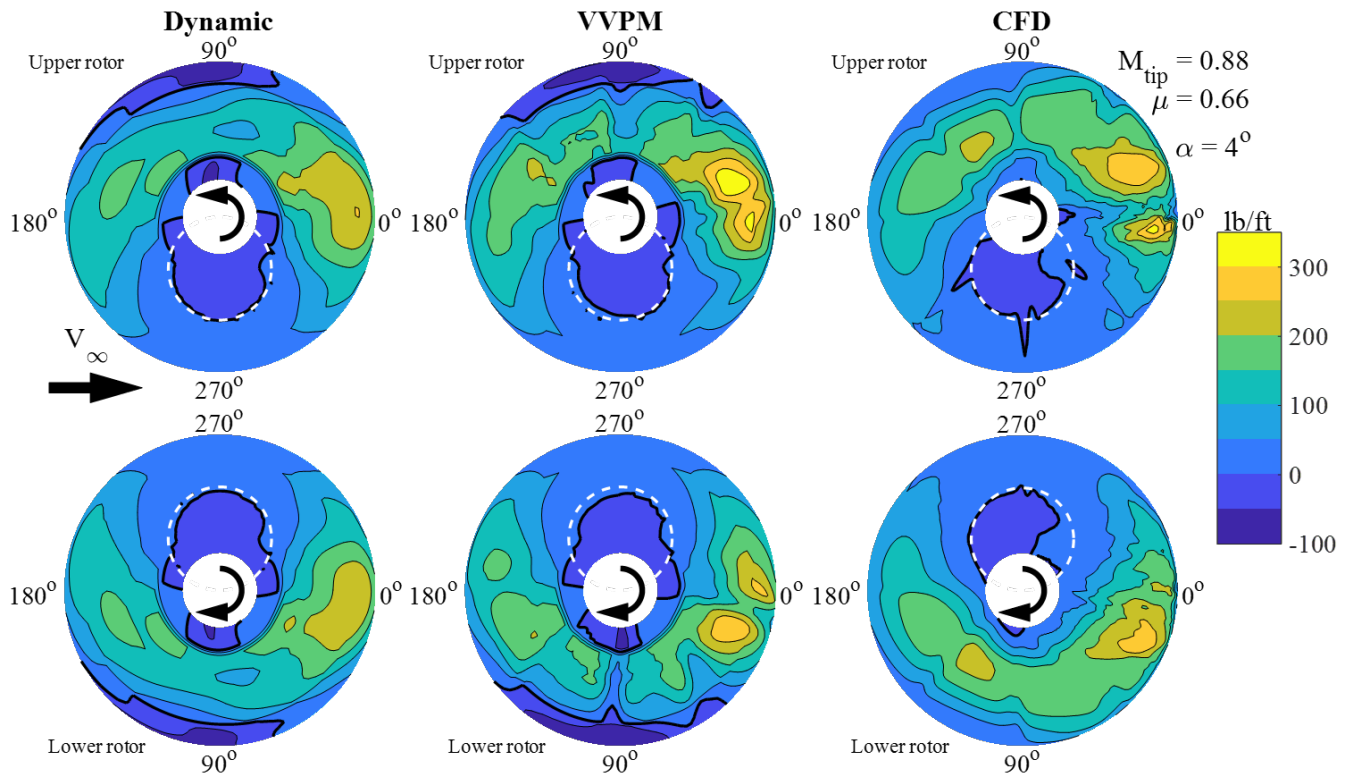


Fig. 18. Lift comparison. Reverse flow region marked in white dashed circle, zero lift line marked by solid black line

than the reduced order models, especially near the blade root. The VPM and CFD also show pulses in the lift every 45 degrees marking the blade passages. These events are absent in the dynamic inflow simulation as the interference model is not sophisticated enough to model this type of interaction. The blade passage events on the retreating side of the upper rotor are particularly strong in the CFD simulation, especially for the upper rotor while they are less prominent in the VVPM simulation.

The blade drag at locations of 25%, 50%, and 75% span is shown in figure 22. Examining the transition into and out of the reverse flow region, (around 230°–310° azimuth at 50% span for example) the reduced order models show large discontinuities in the blade loads corresponding to the angle of attack rapidly changing increasing by 180° as the direction of the flow switches. The CFD simulation shows a smoother transition than the reduced order models, especially at 25% span. The drag at 50% and 75% span is also significantly lower over the advancing side the disk in the CFD simulation. Blade passage, which occurs every 45° results in pulses in the drag, which can be seen in some areas of the CFD and VVPM solutions, although more distinct in the CFD solution.

Figure 23 shows the blade pitching moment at 25%, 50%, and 75% span. Because no pitching moment data was used for the DBLN airfoil in the reduced order models, the loads are zero at 25% span. At 50% and span, the Dynamic inflow and VVPM solutions experience a nose-down pitching moment over most of the disk, reaching a minimum near 90° azimuth and a nose-up moment in the reverse flow region. The CFD

solution at 50% span shows a larger nose-down pitching moment on the advancing side, and a higher nose-up moment in the reverse flow region relative to the reduced order models. The CFD solution also shows relatively large deviations in the pitching moment every 45° as the blades pass, while the VVPM solution shows only very small deviations. At 75% span, The blade section does not enter reverse flow. The pitching moment mostly negative for all three methods. The CFD solution again predicts lower values near 90° azimuth and large deviations every 45° as blade passage occurs.

CONCLUSION

The trimmed flight of the X2 Technology Demonstrator was demonstrated using reduced order models at speeds of up to 250 kt with good comparison to available flight test data. Three different aerodynamic models - Dynamic inflow, Viscous Vortex Particle Method, and Computational Fluid Dynamics - were used to analyze the trimmed flight of the X2 at 230 kt. The airloads were compared, gaining insight into the capability of the 3 different methods.

1. A dynamic inflow model using a cylindrical vortex sheet is able to capture the overall rotor performance and predict the low frequency content of the aerodynamic loads, however lacks the ability to model the details of the rotor to rotor interference and therefore cannot capture events such as blade passage and blade vortex interaction.

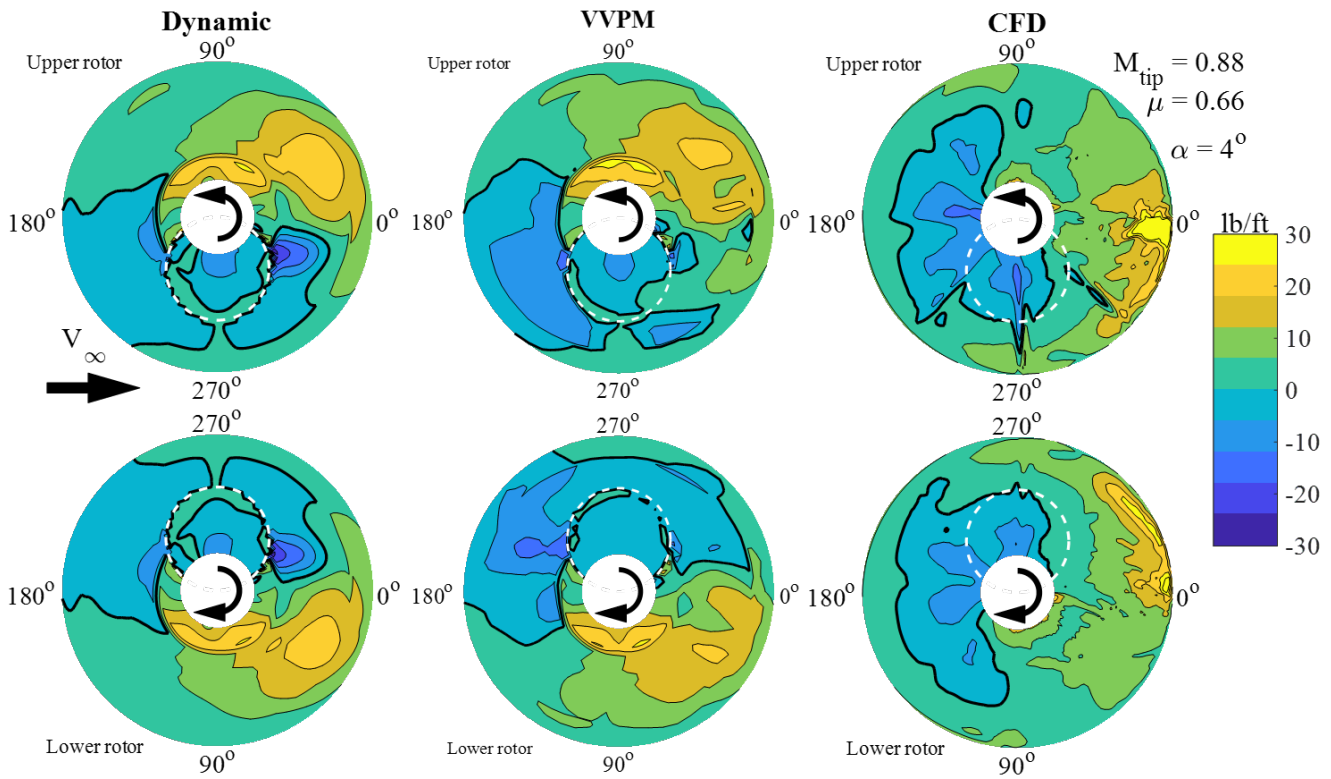


Fig. 19. Drag comparison. Reverse flow region marked in white dashed circle, zero drag line marked by solid black line

2. The Viscous Vortex Particle Method (VVPM) is a physics-based model capturing the most important details of the flow only where necessary via viscous vortex particles. This method can capture events such as blade passage and blade vortex interaction, and requires significantly less setup and runtime than CFD.
3. Both the dynamic inflow and VVPM methods rely on tabulated airfoil data, which only captures the steady performance of airfoil sections at specified conditions. Airfoil sections operating in conditions with large deviations from steady, uniform flow, such as transition into reverse flow, or passing near another blade, are not properly modeled with these methods.
4. Computational Fluid Dynamics (CFD) simulates the full rotor flow field with high resolution and can model transient events such as blade passage and blade vortex interaction with high accuracy, as well as capture the true performance of the airfoil sections as they traverse a highly unsteady and complex flow field (including transition into and out of reverse flow). Proper resolution of the flow requires significant computational resources and runtime. The loads predicted by CFD show deviations from the loads predicted by the reduced order models, particularly as the blade enters and leaves the reverse flow region and as blade passage occurs.

REFERENCES

- ¹Ruddell, A. J., "Advancing Blade Concept (ABCTM) Development," *Journal of the American Helicopter Society*, January 1977.
- ²Ruddell, A., "Advancing Blade Concept (ABC) Technology Demonstrator," Technical report, U. S. Army Research and Technology Laboratories (AVRADCOM), USAVRADCOM-TR-81-D-5, Apr 1981.
- ³Felker, Fort F. III, "Performance and Loads Data from a Wind Tunnel Test of a Full-Scale, Coaxial, Hingless Rotor Helicopter," , October 1981.
- ⁴Phelps, A. E. and Mineck, R. E., "Aerodynamic Characteristics of a Counter-Rotating, Coaxial, Hingeless Rotor Helicopter Model With Auxiliary Propulsion," Technical report, National Aeronautics and Space Administration, NASA Technical Memorandum 78705, 1978.
- ⁵Ruddell, A. J., "XH-59A ABC Technology Demonstrator Altitude Expansion and Operational Tests," Technical Report USAVRADCOM-TR-81-D-35, U. S. Army Research and Technology Laboratories (AVRADCOM), Dec 1981.
- ⁶Pleasants, W. A., "A Rotor Technology Assessment of the Advancing Blade Concept," Technical report, National Aeronautics and Space Administration, NASA Technical Memorandum 84298, 1983.

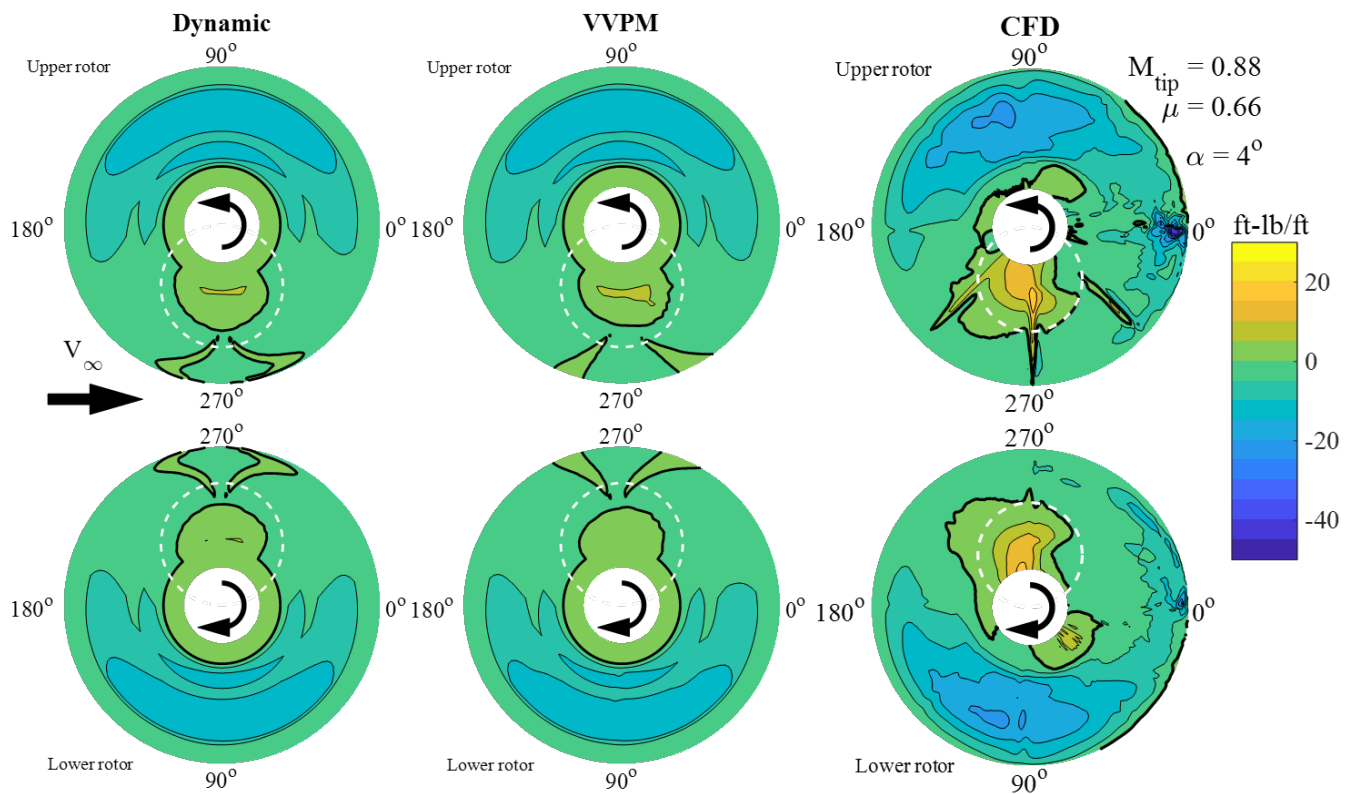


Fig. 20. Pitching moment comparison. Reverse flow region marked in white dashed circle, zero moment line marked by solid black line

⁷O’Leary, J. and Miao, W., “Design of Higher Harmonic Control for The ABC,” *Journal of the American Helicopter Society*, Vol. 27, (1), January 1982, pp. 52–57.

⁸Bagai, A., “Aerodynamic Design of the X2 Technology Demonstrator™ Main Rotor Blade,” 64th Annual Forum of the American Helicopter Society, Montreal, Canada, April 2008.

⁹Blackwell, R. and Millot, T., “Dynamics Design Characteristics of the Sikorsky X2 Technology™ Demonstrator Aircraft,” American Helicopter Society 64th Annual Forum, May 2008.

¹⁰Walsh, D., Weiner, S., Arifian, K., Bagai, A., Lawrence, T., and Blackwell, R., “Development Testing of the Sikorsky X2 Technology™ Demonstrator,” 65th Annual Forum of the American Helicopter Society International, Grapevine, TX, 2009.

¹¹Walsh, D., Wiener, S., Arifian, K., Lawrence, T., Wilson, M., Millott, T., and Blackwell, R., “High Airspeed Testing of the Sikorsky X2 Technology™ Demonstrator,” 67th Annual Forum of the American Helicopter Society International, Virginia Beach, VA, 2011.

¹²Lind, A. H., Lefebvre, J. N., and Jones, A. R., “Time-Averaged Aerodynamics of Sharp and Blunt Trailing-Edge Static Airfoils in Reverse Flow,” *AIAA Journal*, Vol. 52, (12),

December 2014, pp. 2751–2764.
doi: 10.2514/1.J052967

¹³Lind, A. H., Trollinger, L. N., Manar, F. H., Chopra, I., and Jones, A. R., “Flowfield Measurements of Reverse Flow on a High Advance Ratio Rotor,” 43rd Annual European Rotorcraft Forum, Sept. 2017.

¹⁴Hodara, J., Lind, A. H., Jones, A. R., and Smith, M. J., “Collaborative Investigation of the Aerodynamic Behavior of Airfoils in Reverse Flow,” AHS 71st Annual Forum, May 2015.

¹⁵Mayo, M., Raghav, V., and Komerath, N., “Vortex Flow Hypothesis for a Yawed Rotor Blade in Reverse Flow,” 2013 ASME International Mechanical Engineering Congress & Exposition, 2010.

¹⁶Hiremath, N., Shukla, D., Raghav, V., Pirau, S., and Komerath, N., “Effects of Advance Ratio and Radial Location on the Vortex Structure on a Rotating Blade in Reverse Flow,” AHS 71st Annual Forum, 2015.

¹⁷Hiremath, N., Shukla, D., Raghav, V., and Komerath, N., “A Summary of the Flowfield Around a Rotor Blade in Reverse Flow,” AHS 72nd Annual Forum, 2016.

¹⁸He, C. and Zhao, J., “Modeling Rotor Wake Dynamics with Viscous Vortex Particle Method,” *AIAA Journal*, Vol. 47, (4), April 2009.

¹⁹Yeo, H. and Potsdam, M., “Rotor Structural Loads Analysis Using Coupled Computational Fluid Dynamics/Computational Structural Dynamics,” AHS 70th Annual Forum, 2014.

²⁰Johnson, W., Moodie, A. M., , and Yeo, H., “Design and Performance of Lift-Offset Rotorcraft for Short-Haul Missions,” AHS Future Vertical Lift Aircraft Design Conference, 2012.

²¹Kim, H. W., Kenyon, A. R., Brown, R. E., and Duraisamy, K., “Interactional Aerodynamics and Acoustics of a Hingeless Coaxial Helicopter with an Auxiliary Propeller in Forward Flight,” *The Aeronautical Journal*, Vol. 113, (1140), Feb 2009, pp. 65–78.

²²Cameron, C. and Sirohi, J., “Performance and Loads of a Model Coaxial Rotor Part I: Wind Tunnel Testing,” AHS 72nd Annual Forum, 2016.

²³Schmaus, J. and Chopra, I., “Performance and Loads of a Model Coaxial Rotor Part II: Prediction Validations with Measurements,” AHS 72nd Annual Forum, 2016.

²⁴Cameron, C., Sirohi, J., Feil, R., and Rauleder, J., “Measurement of Transient Loads and Blade Deformation in a Coaxial Counter-Rotating Rotor,” AHS International 73rd Annual Forum, 2017.

²⁵Passe, B., Sridharan, A., Baeder, J., and Singh, R., “Identification of Rotor-Fuselage Aerodynamic Interactions in a Compound Coaxial Helicopter using CFD-CSD Coupling,” AHS technical meeting on Aeromechanics Design for Vertical Lift, January 2016.

²⁶Andrew M. Wissink, a. B. J. and Sitaraman, J., “An Assessment of the Dual Mesh Paradigm Using Different Near-Body Solvers in Helios,” 55th AIAA Aerospace Sciences Meeting, 2017.
doi: 10.2514/6.2017-0287

²⁷Jain, R., Yeo, H., Ho, J. C., and Bhagwat, M., “An Assessment of RCAS Performance Prediction for Conventional and Advanced Rotorcraft Configurations,” AHS 70th Annual forum, 2014.

²⁸Johnson, W., “Lift-Offset Compound Design Background, X2TD, JMR ME1A Status and Plans,” , August 2011.

²⁹Jacobellis, G. and Gandhi, F., “Investigation of Performance, Loads, and Vibrations of a Coaxial Helicopter in High Speed-Flight,” AHS 72nd Annual Forum, 2016.

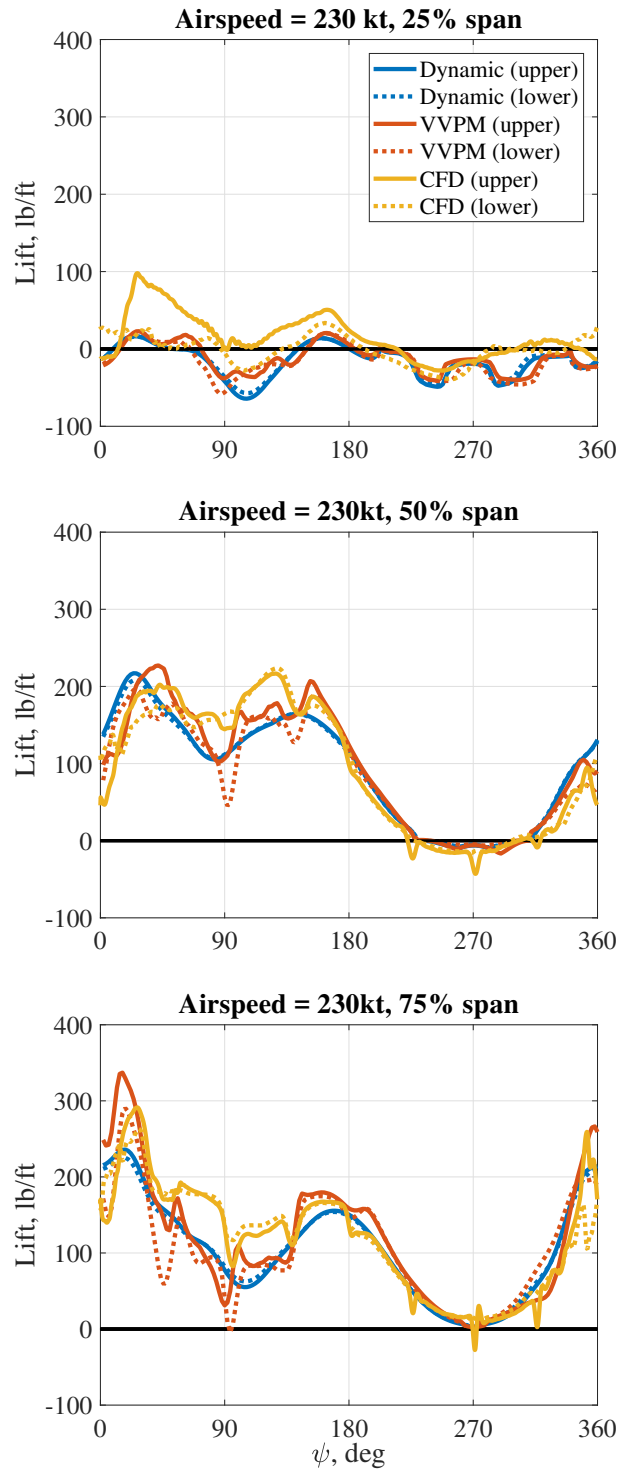


Fig. 21. Blade lift at spanwise locations

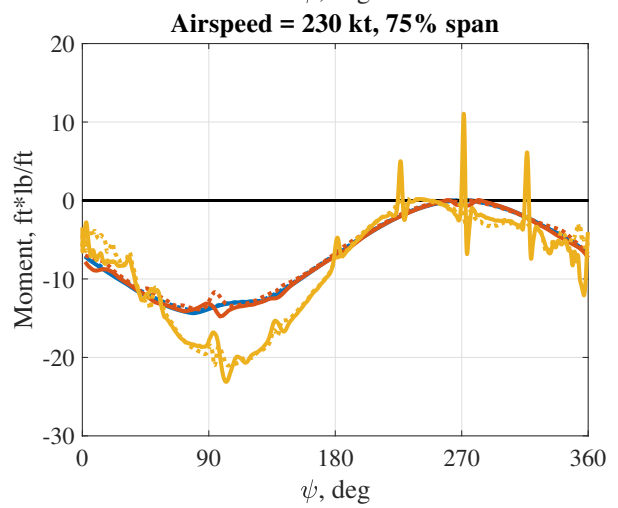
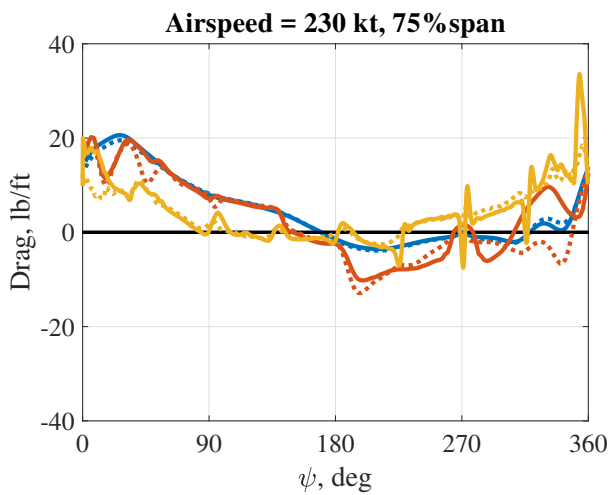
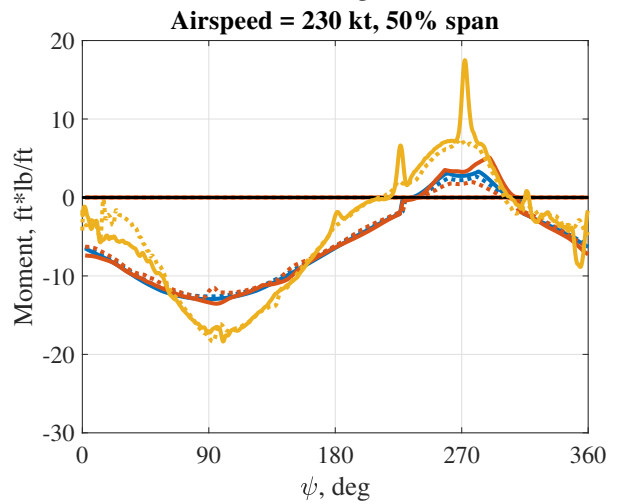
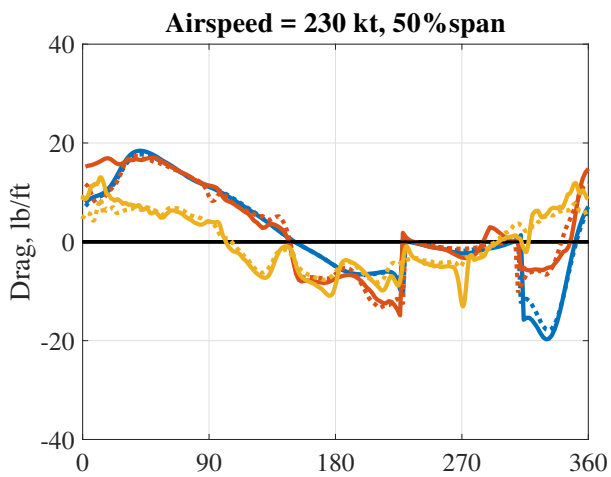
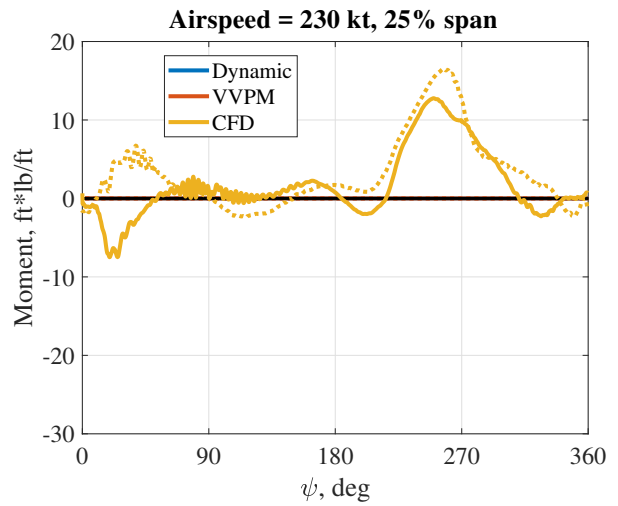
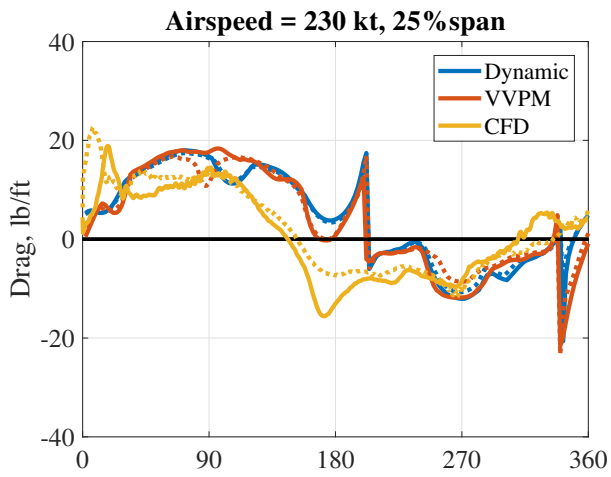


Fig. 22. Blade drag at spanwise locations

Fig. 23. Blade pitching moment at spanwise locations